High Power Laser Science and Engineering, (2024), Vol. 12, e18, 11 pages.
doi:10.1017/hpl.2023.99

HIGH POWER LASER SCIENCE AND ENGINEERING

RESEARCH ARTICLE

A simple method for pulse contrast enhancement via self-focusing

Zaharit Refaeli[1,2], Gilad Marcus[2], and Yariv Shamir[1]

[1]*Applied Physics Division, Soreq NRC, Yavne, Israel*

[2]*Applied Physics Institute, The Hebrew University, The Edmond J. Safra Campus - Givat Ram, Jerusalem, Israel*

(Received 24 August 2023; revised 22 November 2023; accepted 15 December 2023)

Abstract

Here we report on a simple-to-implement and cost-effective approach for laser pulse contrast enhancement, based on the $\chi^{(3)}$ nonlinear self-focusing effect. An intentionally induced and gently controlled self-focusing in a thin glass transforms the time-dependent intensity into variation in beam divergence. Followed by a spatial discriminating filter, only the strongly focused fraction traverses the setup, at the expense of efficiency. A numerical model, accounting for the pulse and material parameters via a Gaussian ABCD matrix, provides an estimate for the instantaneous beam waist and transmission efficiency, which enables us to evaluate the resulting contrast enhancement. The estimated contrast enhancement spans between 0.5 and 2.5 orders of magnitude, in conjunction with approximately 25%–90% estimated efficiency, depending on the pulse parameters. In a preliminary experiment we demonstrated the effect with 10s-μJ sub GW regime with approximately 40% efficiency and a contrast improvement of more than or equal to 20 dB.

Keywords: nonlinear optics; pulse contrast; self-focusing; ultrafast laser

1. Introduction

Since the appearance of high-energy short pulse laser systems based on chirped pulse amplifiers (CPAs)[1], it has become apparent that certain experiments can be hindered by pulse parts that are not confined to the peak vicinity. It is therefore important to define the pulse contrast ratio, that is, the ratio between the peak intensity and intensities extended towards the pulse pedestals. As a result, high-field experiments have made the pulse contrast a property of vast importance. In that context, the most demanding experiments are those involving the interaction of intense light with solids[2,3], as they start to dissociate into plasma. Typically, solid targets experience coulomb explosion under intensities of above 10^{10} and 10^{13} W/cm^2[4] for nanosecond (ns) pedestals or picosecond (ps) pre-pulses, respectively[5]. Once the plasma becomes over-critical, that is, the plasma density scale length increases, interaction is hindered. Hence, when intensities are of the order of $10^{17} - 10^{21}$ W/cm^2, the contrast level must be kept above approximately $10^7 - 10^{11}$.

In recent decades, several techniques have been developed to clean up pulses, most of which are based on instantaneous gating mechanisms obtained by nonlinear (NL) processes. Amongst these are, for example, the cross-polarized wave (XPW)[6], second-harmonic generation (SHG)[7], optical parametric amplification (OPA) and, specifically, optical parametric chirped pulse amplification (OPCPA)[8,9,10], plasma mirrors (PMs)[11,12], self-diffraction (SD)[13,14,15], etc. Methods such as those mentioned above typically clean up pulses by two to five orders of magnitude, with reported values of as much as a 70 dB improvement[16]. As with most NL processes, the above-mentioned cases are associated with a significant energy penalty, that is, efficiencies ranging from tens to a few percent.

An exceptional result was introduced in 2020, with an approach based on a spatial NL plasma lens that was generated by an auxiliary pump beam[17]. While achieving contrast enhancement (CE) of two orders of magnitude, with impressive efficiency of approximately 80%, such a method entails significant awkwardness, as it necessitates slaving a secondary laser into the process and accurately synchronizing it with the main laser.

The approach described in this work is based on a self-induced single-beam effect, which is achieved by simply activating the basic Kerr lens (KL) effect[18] using peak powers significantly beyond the critical peak power for self-focusing (∼4 MW for a Gaussian beam in glass), given a thin enough sample (i.e., before the beam collapse occurs

Correspondence to: Zaharit Refaeli, Applied Physics Division, Soreq NRC, Yavne 8180000, Israel. Email: zaharitre@soreq.gov.il

inside the bulk material[19]) followed by a succeeding spatial filtration. Since the NL lens constitutes temporal-spatial-temporal mapping, the latter filtration translates to temporal cleaning, as elaborated below. Obviously, such a process occurs in-line, is self-induced and requires no alignment to achieve the effect. Although some similarities to the above-mentioned plasma lens exist, the proposed method is far easier to implement since it is a self-induced process and does not require any additional optically synchronized sources or unique materials.

Using the KL in the context of pulse cleaning was investigated in a work published in 1975, in the form of a numerical model that simulated the KL mechanism inside a laser oscillator for CE[20]. However, since the model was based on blocking the center of the beam, it predicted optimal operation only inside oscillators, whereas for amplifier applications it is expected to introduce low efficiency. Naturally, under much higher energies such a process is less attractive. This drawback can, in the present context, be offset by certain variations in the model's scheme, as proposed here. Interestingly, in recent decades, the spatial beam aspect affected by the KL was found to enhance certain laser beam properties. Liu *et al.*[21] demonstrated spatial cleanup, namely M^2 beam parameter reduction via the KL, induced by a short pulse in a multi-mode graded-index fiber. Against most of the CE efforts, intentional reduction of the pulse contrast via the KL effect was demonstrated in 2019[22] with the purpose of measuring high pulse contrast with limited diagnostics. The current study follows an alternative path to the latter, which with some further modification, can achieve pulse CE.

In 2021, an experimental study on the KL effect on CE demonstrated the use of multiple plates and a succeeding filter[23]. This study indeed confirmed the validity of the self-focusing approach for CE. The work presented here proposes a complementary approach, providing both a numerical model and a validation with a single-stage NL element.

2. Kerr lens approach

Here, we propose a method that uses the KL to discriminate between different time-varying pulse intensity levels. In a simplified description, the technique is aimed to improve contrast via gently controlled KL excitation in a relatively thin dielectric, that is, the beam experiences negligible transverse variations while traversing a short path along the dielectric. However, it induces angular convergence, as elaborated below. The method's principle is of translating the time-varying pulse intensity profile to corresponding variations in its spatial dimensions, that is, the beam waist size, and then consecutively applying spatial filtration. The latter spatially modifies parts that traverse the filter, which, in turn, affects its temporal profile.

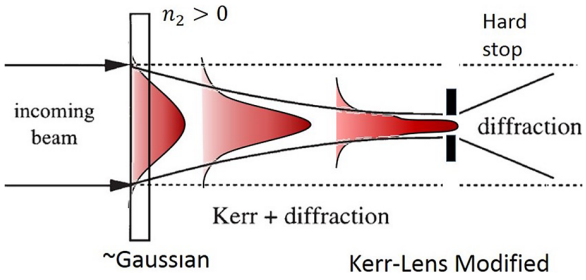

Figure 1. An Illustration showing the spatial shaping of a Gaussian beam affected by the temporal intensity change, which in turn modifies the medium.

It is to be stressed that as a byproduct, the process potentially involves excitation of the NL phase via self-phase modulation (SPM), adding some *B*-integrals as well as positive second-order dispersion to the pulse phase. This implies that in the case in which obtaining the shortest available pulse from the setup is mandatory, some extra dispersion compensation may be required.

The numerical model's concept maintains two assumptions. Firstly, the KL is induced within a relatively thin dielectric ('thin' refers here to negligible beam diameter variations while traversing through the dielectric), that is, the beam only obtains a local angular bend and starts to converge. Naturally, the physical process involves the combination of angular change and some diameter change. The propagation stage where the waist is formatted occurs outside the sample, (i.e., in air or vacuum). As a byproduct, there is a lower risk of further NL accumulation or material breakdown (air ionization starts at $I > 10^{13}$ W/cm^2). Secondly, the instantaneous nature of the NL susceptibility in the dielectric, typically having a sub-femtosecond (fs) delayed response[24], enables pulses that span around multiple tens of fs to ps time to experience instantaneous spatial variations and thereby contrast cleaning regardless of the preceding pulse parts.

Assuming sufficient pulse intensity is available, the underlying mechanism can be described as follows. Initially, low-intensity pulse parts that are temporally far from the main peak nearly maintain their spatial properties as they merely experience any Kerr nonlinearity. As a result, the beam divergence remains practically unchanged when passing the dielectric. In contrast, higher-intensity parts, including the main peak, maintain enough energy to excite the KL, which in turn modifies the beam's angular propagation and, consequently, its diameter. The process is to be kept under gentle control, that is, such that it is far enough from initiating aggressive focusing and material breakdown. Next, a spatial filter is applied such as, for example, an iris/hard aperture, to filter a portion of the Gaussian beam's exterior, as shown in Figure 1.

On the downside, one can list the inevitable addition of the *B*-integral to the pulse phase, potentially adding some

temporal phase structure that temporally broadens the incident pulse by a slight up-chirp. The NL B-integral phase addition can be readily estimated via[25] $B = k_0 \cdot n_2 \int I(z)\mathrm{d}z$, with $k_0 = 2\pi/\lambda_0$, accumulated along the pulse propagation axis inside the dielectric. Some compensation to the B-integral issue can be realized by applying, for example, controlled pulse shaping techniques[26].

It is again pointed out that the assumed applied power level does not lead to total beam collapse and optics damage. Practically, this can be handled by avoiding two distinct criteria: intensities of $I \geq 10^{14}$ W/cm^2 and fluences of more than or equal to 2 J/cm^2 for sub ps pulses[27].

As a last remark, it is reasonable to argue that the suggested method has several potential distinct benefits over the well-known methods due to its ease of implementation, very low-cost components and not requiring the temporal and spatial synchronization of the beams.

3. System schematics

The experimental scheme that exploits the temporal-spatial pulse coupling is presented in Figure 2.

We assume a collimated near-infrared ultrashort pulse with available peak power significantly beyond the dielectric's NL critical power. In the first stage, the beam is focused by a lens with a (linear) focal length f_L. For beam with a divergence angle θ (before the lens), the 4σ waist (after the lens) is $2w_0 \approx f_\mathrm{L} \cdot \theta$, assuming a small angle approximation.

Focusing the beam in the first stage is needed for initiating the NL mechanism, especially in the case of fairly low pulse energies. Furthermore, as shown below, z_glass, the glass distance from the waist, is an additional tuning parameter for the intensity that is provided by delicately moving the glass along the beam.

Next, while the beam enters the NL medium, a new converging beam trajectory is induced by the Kerr effect, whose focal length can be calculated (assuming Gaussian intensity shape) by the following equation[28]:

$$f_\mathrm{NL}^{-1} = \frac{8n_2 d}{\pi w^4} P, \tag{1}$$

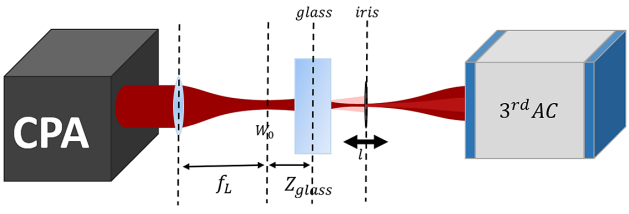

Figure 2. System schematic. f_L, linear focal length; w_0, beam waist after the lens; z_glass, glass distance from beam waist; l, iris-to-glass distance (movable); 3rd AC, third-order scanning autocorrelator.

where n_2 is the NL refractive index, d is the glass thickness, w is the beam radius and P is the instantaneous laser power. Moving the glass piece with respect to the beam waist position (z_glass) raises several scenarios that can be roughly divided into the following categories, depending on the generated NL focal length f_NL:

(1) the NL dielectric is located at $z_\mathrm{glass} = f_\mathrm{NL}$, precisely compensating the linear lens power, yielding a collimated beam (Figure 3(a));

(2) the NL dielectric is located at $z_\mathrm{glass} < f_\mathrm{NL}$, not compensating the linear lens and leading to a diverging beam (Figure 3(b));

(3) the NL dielectric is located at $z_\mathrm{glass} > f_\mathrm{NL}$, refocusing and generating a new (NL) beam waist (Figure 3(c)).

The temporal cleaning method provided in this study is based on spatial separation, practically achieved via the presence of an aperture. Looking at the three scenarios illustrated in Figure 3, it is argued that the highest area ratio between the peak (dark red) and the noise (light red) is obtained in case (3), and at the tightest NL focus. The area ratio is as follows:

$$\frac{A'_\mathrm{peak}}{A'_\mathrm{noise}} = \frac{C^2 + 2C^2\frac{l(N-1)}{z_\mathrm{glass}} + C^2\frac{l^2(N-1)^2}{z_\mathrm{glass}^2}}{C^2 + \left(l + z_\mathrm{glass}\right)^2} + \\ + \frac{z_\mathrm{glass}^2 + 2lNz_\mathrm{glass} + l^2N^2}{C^2 + \left(l + z_\mathrm{glass}\right)^2}, \tag{2}$$

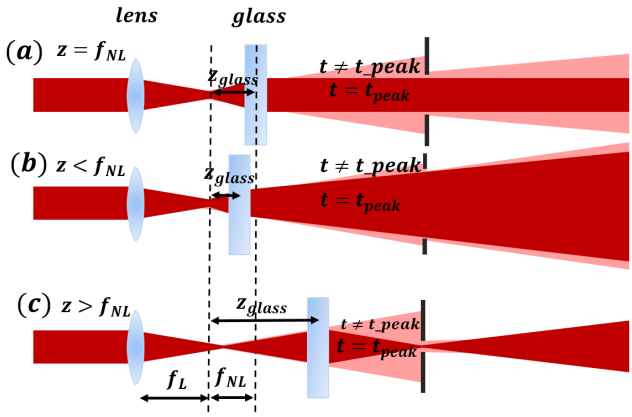

Figure 3. Illustration of the three KL focusing scenarios, obtained by varying the dielectric location with respect to the beam waist: (a) $z_\mathrm{glass} = f_\mathrm{NL}$, (b) $z_\mathrm{glass} < f_\mathrm{NL}$ and (c) $z_\mathrm{glass} > f_\mathrm{NL}$. f_L, linear lens focal length; f_NL, NL lens focal length. The dark red part represents the peak of the pulse where most of the NL process occurs, whereas the light red part represents lower powers and noises adjacent to the peak with the weaker effect.

A crucial parameter that is, to our approach, used as a metric for the contrast change, is the peak-to-noise area ratio at the hard aperture filtration plane. This metric shall be an estimate to the filtering ratio that finally can be related to CE.

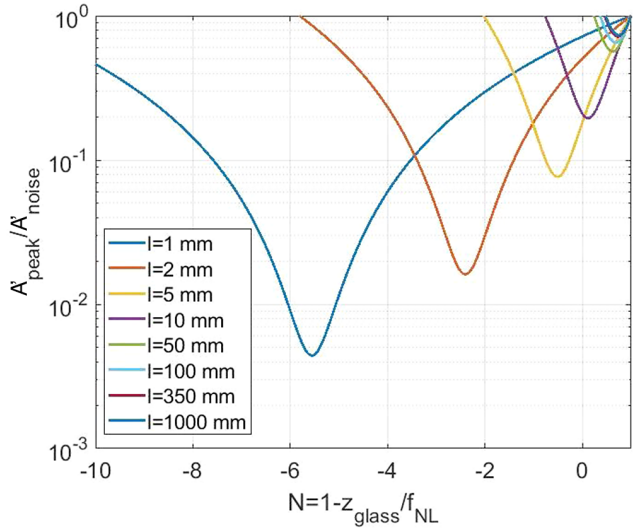

Figure 4. Peak-to-noise beam area ratios under various iris-to-glass distances (l) versus N values of z_{glass} and C, which were set to 6.3 and 10.7 mm, respectively.

where $A=\pi w^2$, $C=\pi w_0^2/\lambda$ and l is the iris distance from the glass. Here, N is defined as $N=1-z_{glass}/f_{NL}$. Note that $N=0$, $N>0$ and $N<0$ refer to cases (1), (2) and (3), respectively. The full calculation is detailed in Appendix A.

As obtained from Figure 4, for a given C (10.7 mm) and z_{glass} (6.3 mm) (according to the system parameters provided in Section 4) and various l values, the ratio of A'_{peak}/A'_{noise} has a minimum. When traveling long distances (l of approximately meters scale), these minima are found around $N=0$, that is, $\Rightarrow f_{NL}=z_{glass}$, corresponding to case (1), whereas if traveling small distances (l of a few millimeters scale), the minima are found around $N<0$, that is, $\Rightarrow f_{NL}<z_{glass}$, which corresponds to case (3). In addition, for shorter iris–glass distances (l), the area-ratio minima values (the local dips in Figure 4) further reduce with lower N values, that is, pointing to a potentially valuable CE trend. By setting the expressions of the latter cases, one can claim that the $f_{NL}<z_{glass}$ case is optimal for discriminating between A'_{peak} and A'_{noise}, and therefore the potential for CE is reinforced. It is therefore that in this work the most appealing approach to expect CE is under the conditions of case (3), which indeed was selected.

By inserting the explicit expressions $N(z_{glass})=1-z_{glass}/f_{NL}$ and $f_{NL}(z_{glass})=B\left(1+(z_{glass}/C)^2\right)^2$, where $B=\left(\pi w_0^4\right)/(8n_2dP)$ into Equation (2), the following expression is obtained (see Appendix B):

$$A'_{peak}/A'_{noise}=\frac{C^4l\left(C^4l-2B\left(C^2+z_{glass}^2\right)\left(C^2+z_{glass}\left(l+z_{glass}\right)\right)\right)}{B^2\left(C^2+z_{glass}^2\right)^3\left(C^2+\left(l+z_{glass}\right)^2\right)}+1, \tag{3}$$

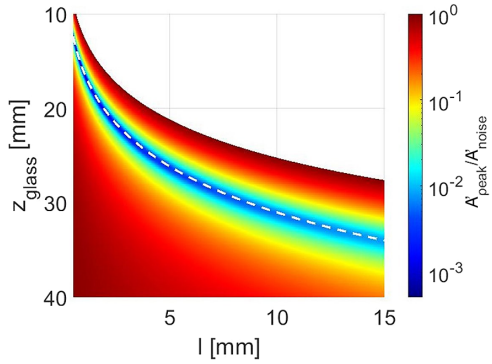

Figure 5. Two-dimensional plot showing the peak-to-noise area ratio versus l and z_{glass}. White dashed curve: $l=z_{w_{0,NL}}$.

Obviously, one may seek a case where the smallest A'_{peak}/A'_{noise} ratio as a function of glass–iris distance (l) as well as an NL medium (glass) position (z_{glass}) can be obtained. A plot of Equation (3) is shown in Figure 5 via a 2D representation.

In addition, the location of the newly formed waist at the pulse peak ($z_{w_{0,NL}}$) can be expressed as follows (further details in Appendix B):

$$z_{w_{0,NL}}=\frac{z_{glass}-f_{NL}}{\left(1-z_{glass}/f_{NL}\right)^2+\left(\frac{2C}{\pi f_{NL}}\right)^2}+f_{NL}. \tag{4}$$

The expression in Equation (4) is represented by the white dashed curve in Figure 5. It can be seen that the white line is located exactly on the minimum of A'_{peak}/A'_{noise}, proving the basic estimation provided above that the iris optimal location is at the NL peak waist location $z_{w_{0,NL}}$.

Given the latter outcome, the hard aperture iris was selected to be positioned at the very spot where the KL-induced waist position occurs: $l=z_{w_{0,NL}}$.

It is worth noting that in order to apply the model's initial assumption for thin glasses, $z_{w_{0,NL}}$ must have a lower boundary with respect to the glass thickness d. Assuming up to 10% beam diameter narrowing from the initial value, running a beam propagation code that tracks the spatial pulse dynamics[29], the aforementioned requirement is satisfied under the limit (see Appendix C): $z_{w_{0,NL}}>d/2$. Thus, this limit is used in what follows according to the presented model.

In another aspect, the iris aperture size constitutes a trade-off between efficiency and CE, since a larger aperture transmits more energy whereas a smaller aperture increases CE.

At low intensities, the iris blocks the majority of the emerging beam as its diameter (and area) is smaller relative to the pulse beam area at this position. In contrast, near the intensity peak, the majority of the beam energy is confined

to the NL waist w_{NL}, and efficiently traverses the iris, that is, it experiences minimal attenuation.

4. Numerical model

In this section, a numerical model with parameters resembling those of the available laser system was established to evaluate the expected CE.

Temporal and spatial Gaussian shapes were assumed. Next, some temporal noise features were artificially added to the pulse vicinity in order to represent non-ideal contrast. The noise levels are specified below. The time profile included, firstly, a sharp peak of a few hundred fs duration that is typical for Yb-doped glass amplifiers, accompanied by a time-exponential coherent pedestal (CP) that is typically reported to surround the peak vicinity by several 10 ps. While presented on a power scale, the CP has a linear skirt-like shape (Figure 6). A lower noise pedestal was also introduced to represent the longer-term amplified spontaneous emission (ASE) noise in the amplifiers. This noise level typically spans multi-hundred ps from both sides of the peak.

In recent decades, studies have pointed out that the CP is attributed mainly to grating irregularities and scattering found, for example, on the groove edges[30], as well as imperfections in the (whole) stretcher and compressor structures.

Based on reports[31,32] and experience with CPA lasers, the CP and ASE were chosen in our model to have a level of –25 and –50 dB relative to the pulse peak.

The parameters that were used in the numerical model are as follows: pulse energy $E = 1$ mJ, central wavelength CWL = 1053 nm, divergence angle $\theta = 2$ milli-radian (mrad) and a time duration of 450 fs full width at half maximum (FWHM). The numerical temporal pulse shape is presented on a power scale in Figure 6. In our example case, the power at the pulse's peak is approximately 0.664 GW after being adjusted to the chosen energy such that $\int P(t)\mathrm{d}t = E$, where $P(t)$ and E are the power and total pulse energy, respectively.

In order to determine the appropriate z_{glass}, f_{NL} as a function of z_{glass} was calculated, based on Equation (1). The beam waist at the glass position was derived from the following:

$$w(z) = w_0\sqrt{1+\left(\frac{\lambda\cdot z}{\pi\cdot w_0^2}\right)^2},$$

where $w_0 \simeq \theta\cdot f_L/2$ while P was assumed to be the pulse peak power.

The resulting NL focal length as a function of z_{glass} is represented by the blue curve in Figure 7. In order to visualize the three different cases discussed above, $f = z_{glass}$ is plotted in Figure 7 (orange curve). According to Figure 7, z_{glass} has to fall within the range of 0–52 mm in order to preserve the condition $f_{NL} < z_{glass}$. The simulation's input parameters were $f_L = 60$ mm, $d = 1$ mm, $\theta = 2$ mrad and $n_2 = 2.6\times10^{-20}$ m^2/W (typical to fused silica around 1 μm).

To obtain the optimal beam areas ratio, it is beneficial to follow the A'_{peak}/A'_{noise} curve ($l = z_{w_{0,NL}}$, z_{glass}) and seek for a minimum, according to Equation (3) at $l = z_{w_{0,NL}}$ (Equation (4)). As presented in Figure 8, z_{glass} was chosen to be 6.3 mm.

Since in real scenarios it is not always possible to work at extremely short distances, or extremely small apertures, a slightly larger z can be chosen in order to shift the NL focal position, or enlarge the NL focal size.

In what follows, calculation of the NL focal length versus time is provided, where Equation (1) is applied with the optimal z_{glass} (6.3 mm). It can be inferred from Figure 9 that f_{NL} varies from sub 0.5 mm at the pulse's peak, which indicates an extremely intense effect, to approximately 1 m, when the laser power reduces below P_{cr}. Farther out, at tens

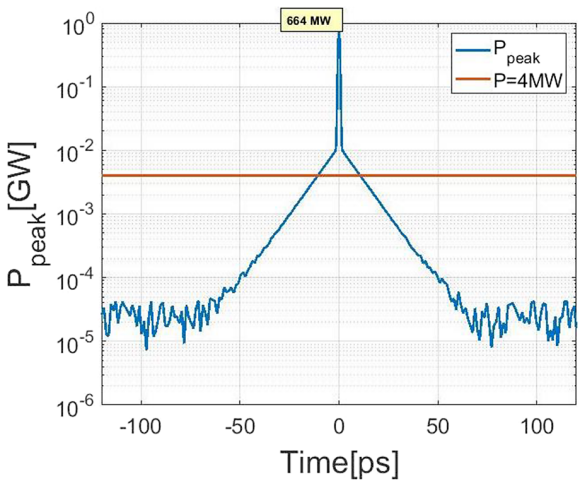

Figure 6. Pulse power versus time. Blue, numerically produced contrast trace of power versus time, on a normalized power scale. Orange, a reference 4 MW power level.

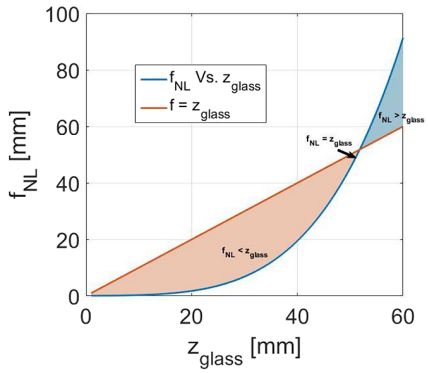

Figure 7. Kerr focal length as a function of glass distance from the beam waist position (blue), crossed with the linear $f = z_{glass}$ plot (orange). The intersection point of the two plots represents the precisely collimated case.

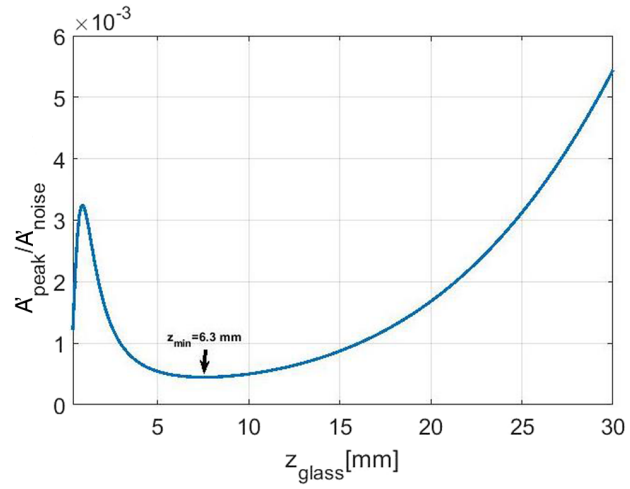

Figure 8. Beam area peak-to-noise ratio $A'_{\text{peak}}/A'_{\text{noise}}$ at $l = z_{w_{0,\text{NL}}}$, where the minimum ratio is obtained at $z_{\text{glass}} = 6.3$ mm.

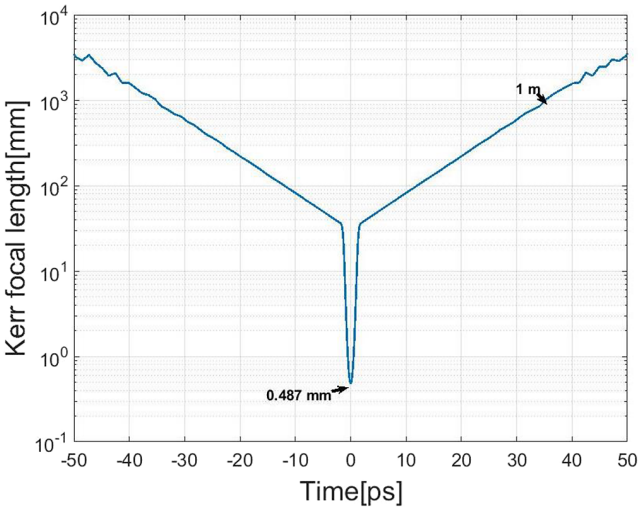

Figure 9. Kerr focal length as a function of time, based on the numerical pulse from Figure 6 (blue).

of ps, f_{NL} extends to much larger values, practically implying a negligible effect.

In order to estimate the spatial filtration effect, the NL beam waist diameter was calculated as well as the NL-induced waist position (with respect to the NL dielectric) according to the Gaussian beam propagation equation[33]:

$$z_{w_{0,\text{NL}}}(t) = \left(\left(\frac{w_{0_{\text{NL}}}(t)}{w_0}\right)^2 \cdot \left(|z| - f_{\text{NL}}(t)\right)\right) + f_{\text{NL}}(t), \qquad (5)$$

where the NL waist $w_{0_{\text{NL}}}$ is obtained by the following:

$$w_{0_{\text{NL}}}(t) = \frac{w_0}{\sqrt{\left(1 - \frac{z}{f_{\text{NL}}(t)}\right)^2 + \left(\frac{z_0}{f_{\text{NL}}(t)}\right)^2}}, \qquad (6)$$

and $z_0 = \pi w_0^2/\lambda$ is the Rayleigh length produced by the linear lens.

The calculated position of the new waist at the peak ($t = 0$) was $z_{w_{0,\text{NL}}}(t = 0) = 0.5$ mm for the resulting f_{NL} mentioned above. It is noted that the waist position turned out to be slightly larger ($f_{\text{NL}} \sim 0.48$ mm) as a result of the preceding divergence. To obtain the strongest NL gating discrimination (for the specific chosen parameters) as explained in the preceding section, the position of the hard aperture filtering was set to be $z_{w_{0,\text{NL}}}(t = 0)$.

Next, the instantaneous beam radii, obtained at the iris plane, were calculated using the following equation:

$$w\left(z = z_{w_{0,\text{NL}}} - z_{w_{0,\text{NL}}}(t = 0), t\right) = w_{0_{\text{NL}}}(t)\sqrt{1 + \left(\frac{z_{w_{0,\text{NL}}}(t) - z_{w_{0,\text{NL}}}(t = 0)}{z_{0_{\text{NL}}}(t)}\right)^2}, \qquad (7)$$

where z was selected to be the distance between the iris plane ($z_{w_{0,\text{NL}}}(t = 0)$) and the time-dependent NL beam waist, and $z_{0_{\text{NL}}}$ is the NL Rayleigh length induced by that same Kerr effect.

Following the calculated waists $w_{0_{\text{NL}}}$, a 2D spatial-temporal Gaussian beam shape was generated. The spatial part can be described as follows:

$$I(x, y) = I_{0,0}(t) e^{\left(-2\cdot\left(x^2+y^2\right)/w\left(z_{w_{0,\text{NL}}}(t=0),t\right)^2\right)}, \qquad (8)$$

where $I(t)$ is the time pulse intensity.

The sum of all time frames at the iris plane is represented in Figure 10. As can be seen, the final shape resembles a Gaussian one, albeit with a somewhat sharper center.

In order to simulate the hard aperture spatial effect, a 2D circle with varying radii was (numerically) spatially multiplied by the 2D beam shape, in different pulse times. Figure 11 represents this projection on the x-axis at different times (colorful plots), while the iris itself is represented by the black rectangle. As can be observed, the spatial pulse generated at $t = 0$ (Figure 11 in yellow) practically completely traverses the aperture, whereas the spatial pulse preceding the peak by $t = -61.6$ ps (Figure 11 in purple) or earlier suffers a considerable blocking.

5. Results

A two-stage computation was carried out in order to produce the temporal pulse profile following the spatial filtration. The iris aperture and the pulse beam shape were first spatially multiplied, and then the beam's spatial domain was integrated, $I(t) = \int\int I(x, y, t)\,dxdy$, to preserve only temporal dependence. Displaying the latter with unity normalization on the power scale provided the temporal contrasts for four

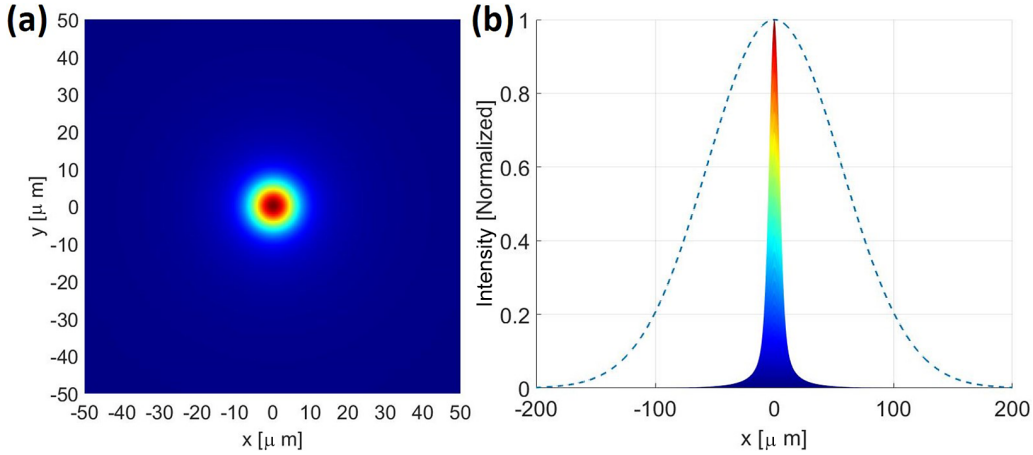

Figure 10. Sum of the 2D generated Gaussians at the iris plane from the top (a) and side views (b). The dashed curve represents the normalized pulse shape assuming no NL effect.

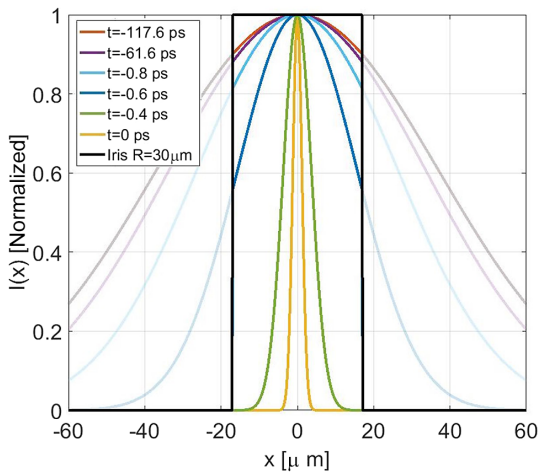

Figure 11. Spatial Gaussian pulses after experiencing the NL lens projected at the iris plane. The colored curves represent spatial pulses at various times. The (numerical) iris is represented by the black curve.

different aperture sizes. The resultant plots are shown in Figure 12.

In addition, in order to complete the performance estimation, the whole process's efficiency was calculated by extracting the ratio of the transmitted energy to the incident energy, using the following integration:

$$\eta = \frac{\int P_{\text{clipped}} \mathrm{d}t}{\int P_{\text{in}} \mathrm{d}t}, \tag{9}$$

where the integral limits in the current work were taken to within the pulse FWHM.

The aforementioned integration was carried out using a variety of aperture radii, considered in ascending order, from largest to smallest, associated with highest-to-lowest transmission, respectively.

For aperture diameters of 70, 34, 10.6 and 4.8 μm, the obtained CE factors were 5, 10, 20 and 25 dB, with corresponding efficiencies of 90%, 74%, 44% and 23% (within the FWHM pulse range) (Figure 12). Considering different energy integration criteria, for example, 10% power drop yields somewhat different efficiencies, 82%, 64%, 36% and 19%, for the same iris diameters, respectively. Of course, as the application demands, various energy integration criteria can be set.

It is, however, stressed that the peak vicinity has a pronounced effect on the experiment, and thus a longer time consideration can be of a lesser value.

It is worth mentioning that according to the simulation results, it can be concluded that a need for small apertures may be impractical. A simple way around this obstacle is applying a magnification (e.g., an imaging stage), allowing the use of larger apertures in a real experiment.

Next, an experimental setup was set in order to validate the applicability of the above model. A full description of the experimental system can be found in Section 3.

The laser setup parameters are as follows: a Yb fiber CPA with a center wavelength of $\lambda = 1.03$ μm, pulse duration of approximately 450 fs (FWHM), a 4σ divergence angle of $\theta = 2.3$ mrad at the output of the CPA's compressor and controlled pulse energies of up to several tens of μJ.

A baseline reference contrast was set as the raw unfiltered CPA pulses, which is needed to be compared with respect to pulses that experienced the NL effect, as proposed in the model. For evaluating the results, a third-order scanning autocorrelator (AC) was used (Ultrafast-Innovations 'Tundra') with optical hardware dedicated to the 1 μm vicinity[34].

According to the experimental results that are plotted in Figure 13, the original laser pulses yielded contrast values of around 10^4 with respect to the noise level, when observed

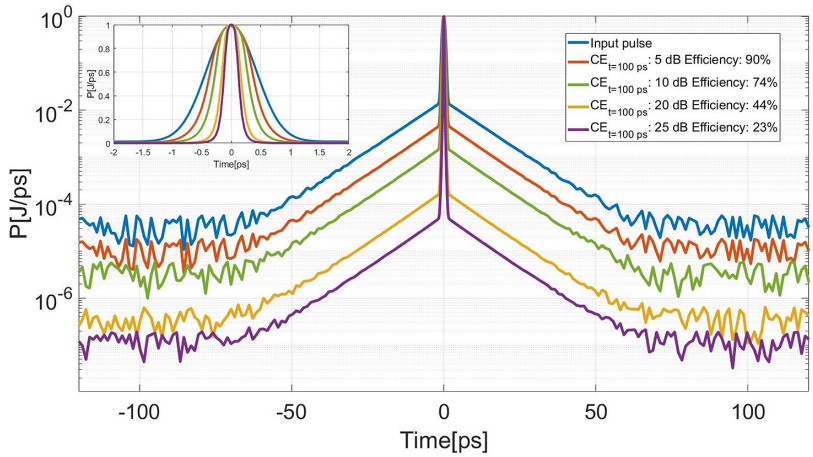

Figure 12. Contrast traces before (blue) and after the KL effect and hard aperture filter, for 70 (orange), 34 (green), 10.6 (yellow) and 4.8 μm (purple) aperture diameters, applied upon the numeric Gaussian input beam. Inset: same plots in the time scale of a few ps surrounding the peak, provided for a more detailed observation.

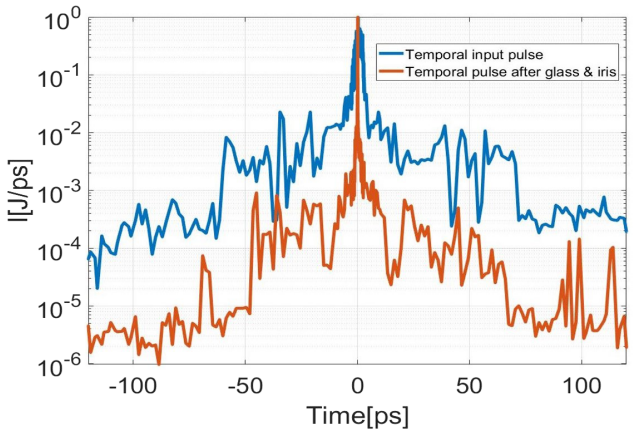

Figure 13. Measured pulse contrast before (blue) and after the KL effect and the clipping aperture (orange).

±100 ps farther away from the peak, which is very typical for Yb fiber CPA laser systems. Further details of the scheme are provided in the following text. The linear lens's focal length f_L was selected to be 100 mm and the NL dielectric piece was 0.25 inch of uncoated fused silica. The output pulse measured after the KL and a 400 μm iris aperture is represented by the orange curve in Figure 13, where the laser input energy $E = 10.5$ μJ, glass location $z_{glass} = 3$ mm and iris location $l = 7$ mm. As shown, the pulse contrast was increased by nearly two orders of magnitude to approximately 10^{-6}, while the measured efficiency (estimated via average power) was 40% using uncoated glass (an additional 8% efficiency can be excepted).

As for the NL phase induced by the setup, the given parameters yield approximately 1 radian, which hardly disrupts the time pulse shape and therefore its contrast as well.

It should be noted that in the experiment, lower pulse energies and therefore thicker glasses were applied, with reference to the model's example. It is to be stressed out that at this early stage of the study, the model refers to a simplified mechanism in which intra-glass beam variations were negligible. In a succeeding work, a more mature model shall cover more complexities, including the processes accumulated within the glass. Such progress shall enable one to validate the experiment more accurately. In addition, an energy upgrade of the scheme shall enable one to operate with thinner glasses and meet cases more overlapping with the numerical model.

6. Conclusions

To conclude, a cost-effective concept for CE based on the KL is proposed. Its attractiveness is based mainly on its simplicity and small number of components, basically an NL glass piece followed by a hard aperture. By correctly placing the components in accordance with specific pulse parameters, the effect can be enhanced. An underlying theoretical and numerical description was provided and expressed via formulas and numerical support. The method is based on the temporal dependence of the NL effect. This dependence is transformed into a spatial one, which is manifested back to provide a cleaner time profile. While a new spatial beam waist is created at the time-peak of the pulse (under certain conditions of $z < f_{NL}$), the weaker and noisy parts, farther from it, hardly induce any spatial changes. Therefore, while the peak traverses the aperture almost entirely, the noisy (weaker) part experiences strong losses, resulting in an overall CE. The current numerical model works as follows: it translated the instantaneous pulse's intensity into 2D spatial

beam distribution variations, followed by 2D multiplication by a hard clip circular aperture. Finally, data is returned to the time domain by spatial integration. In comparison to other CE techniques (e.g., OPA, XPW), one can realize the attractiveness of the proposed approach, considering the overall combination of CE degree, efficiency and low cost. The model predicts typical efficiencies that vary between, for example, 90% for 5 dB CE and 23% for 25 dB CE. In addition, we conducted an experiment that confirmed the numerical result, and demonstrated two orders of magnitude CE at the expense of 40% efficiency. As a final remark, it is further stressed that the technique is simple to implement, not requiring beam synchronization or exotic materials. Therefore laser labs can be considered to benefit from a CE upgrade with good efficiency, that is, to operate high-energy CPA systems with better performance. Further planned studies are underway: one aims at expanding the numerical model to cover thick glasses while the other aims at empirically testing the model under higher energies and different glass thicknesses.

Appendix A. Beam area calculation for pulse peak versus noise for the three cases

A calculation for the beam area, assuming the formation of an NL lens in the glass with a focal length f_{NL}, at the pulse's peak is presented below.

A Gaussian beam can be described by a complex parameter q, which contains information both of the beam radius w and wave-front radius of curvature R[35]:

$$\frac{1}{q} = -i\frac{\lambda}{\pi w^2} + \frac{1}{R}.$$

As can be seen in Figure 14, q is taken to be at the linear lens focal plane f_L; hence, $R \Rightarrow \infty$ and $w = w_0$:

$$\Rightarrow q = i\frac{\pi w_0^2}{\lambda} = iC.$$

It is now possible to apply the ABCD matrix technique for evaluating the pulse peak spatial propagation in the NL process:

$$\begin{pmatrix} A_{peak} & B_{peak} \\ C_{peak} & D_{peak} \end{pmatrix} = \begin{pmatrix} 1 & l \\ 0 & 1 \end{pmatrix} \cdot \begin{pmatrix} 1 & 0 \\ -1/f_{NL} & 1 \end{pmatrix} \cdot \begin{pmatrix} 1 & z_{glass} \\ 0 & 1 \end{pmatrix},$$

that is

$$\begin{pmatrix} A_{peak} & B_{peak} \\ C_{peak} & D_{peak} \end{pmatrix} = \begin{pmatrix} 1 - l/f_{NL} & z_{glass} + l - z_{glass}l/f_{NL} \\ -1/f_{NL} & 1 - z_{glass}/f_{NL} \end{pmatrix}.$$

Let us define a variable, $N = 1 - z_{glass}/f_{NL}$ [$\Rightarrow 1/f_{NL} = (1-N)/z_{glass}$], according to which negative N values express $z_{glass} > f_{NL}$ (case (3) in Section 3), and vice versa. Further developing the latter yields the following:

$$\begin{pmatrix} A_{peak} & B_{peak} \\ C_{peak} & D_{peak} \end{pmatrix} = \begin{pmatrix} 1 + \frac{l(N-1)}{z_{glass}} & z_{glass} + lN \\ \frac{N-1}{z_{glass}} & N \end{pmatrix},$$

$$q'_{peak} = \frac{A_{peak}q + B_{peak}}{C_{peak}q + D_{peak}},$$

where q' represent the Gaussian beam at the iris location, as can be observed in Figure 14. By definition

$$\frac{1}{q'_{peak}} = -i\frac{\lambda}{\pi w'^2_{peak}} + \frac{1}{R'_{peak}},$$

the following can be inferred:

$$\Rightarrow A_{peak} = -\frac{\lambda}{\mathrm{Im}\left(1/q'_{peak}\right)},$$

where $A'_{peak} = \pi w'^{\,2}_{peak}$,

$$\frac{1}{q'_{peak}} = \frac{C_{peak}q + D_{peak}}{A_{peak}q + B_{peak}}.$$

Comparing only the imaginary parts:

$$\mathrm{Im}\left(\frac{1}{q'_{peak}}\right) = \mathrm{Im}\left(\frac{C_{peak}q + D_{peak}}{A_{peak}q + B_{peak}}\right) =$$

$$= \mathrm{Im}\left(\frac{C_{peak}iC + D_{peak}}{A_{peak}iC + B_{peak}}\right) =$$

$$= \mathrm{Im}\left(\frac{(C_{peak}iC + D_{peak})(-A_{peak}iC + B_{peak})}{(A_{peak}iC + B_{peak})(-A_{peak}iC + B_{peak})}\right)$$

$$= \mathrm{Im}\left(\frac{C_{peak}A_{peak}C^2 - iCD_{peak}A_{peak}}{A^2_{peak}C^2 + B^2_{peak}}\right) +$$

$$\mathrm{Im}\left(\frac{iCC_{peak}B_{peak} + D_{peak}B_{peak}}{A^2_{peak}C^2 + B^2_{peak}}\right) =$$

$$= C\frac{C_{peak}B_{peak} - D_{peak}A_{peak}}{A^2_{peak}C^2 + B^2_{peak}},$$

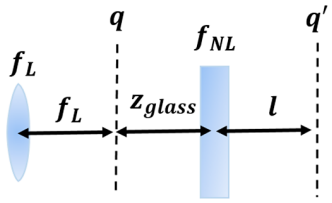

Figure 14. Diagram description of the system precisely at the pulse peak time point, when a nonlinear lens with a focal length f_{NL} is produced. f_L, linear focal length (converging lens); z_{glass}, glass distance from beam waist (w_0); l, distance from the glass where the area ratio is evaluated (also, this is the iris aperture location).

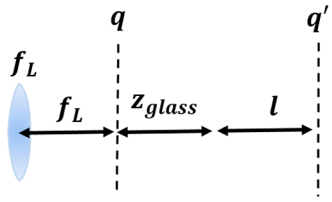

Figure 15. System diagram describing the low pulse intensities and noise, where one assumes no generation of a nonlinear lens f_{NL} in the glass. f_{L}, linear focal length; z_{glass}, glass distance from beam waist (w_0); l, distance from the glass where the areas ratio was evaluated (also this is the aperture position).

therefore,

$$A'_{\mathrm{peak}} = -\frac{\lambda}{C}\frac{A^2_{\mathrm{peak}}C^2+B^2_{\mathrm{peak}}}{C_{\mathrm{peak}}B_{\mathrm{peak}}-D_{\mathrm{peak}}A_{\mathrm{peak}}} =$$
$$-\frac{\lambda}{C}\frac{\left(1+\frac{l(N-1)}{z_{\mathrm{glass}}}\right)^2C^2+(z_{\mathrm{glass}}+lN)^2}{\left(\frac{N-1}{z_{\mathrm{glass}}}\right)(z_{\mathrm{glass}}+lN)-N\left(1+\frac{l(N-1)}{z_{\mathrm{glass}}}\right)} \Rightarrow$$
$$A'_{\mathrm{peak}} = \lambda C+2\lambda C\frac{l(N-1)}{z_{\mathrm{glass}}}+\lambda C\frac{l^2(N-1)^2}{z^2_{\mathrm{glass}}}+$$
$$+\frac{\lambda}{C}z^2_{\mathrm{glass}}+2lN\frac{\lambda}{C}z_{\mathrm{glass}}+\frac{\lambda}{C}l^2N^2.$$

In addition, a computation of the beam area farther from the pulse vicinity (noise) is shown below, assuming no NL lensing occurs within the glass (Figure 15):

$$\begin{pmatrix}A_{\mathrm{noise}} & B_{\mathrm{noise}}\\ C_{\mathrm{noise}} & D_{\mathrm{noise}}\end{pmatrix} = \begin{pmatrix}1 & l\\ 0 & 1\end{pmatrix}\cdot\begin{pmatrix}1 & z_{\mathrm{glass}}\\ 0 & 1\end{pmatrix} = \begin{pmatrix}1 & l+z_{\mathrm{glass}}\\ 0 & 1\end{pmatrix}.$$

Therefore, since $q = iC$, as mentioned above:

$$q'_{\mathrm{noise}} = \frac{A_{\mathrm{noise}}q+B_{\mathrm{noise}}}{C_{\mathrm{noise}}q+D_{\mathrm{noise}}} = iC+l+z_{\mathrm{glass}},$$
$$A'_{\mathrm{noise}} = \pi w'^2_{\mathrm{noise}} = -\lambda\cdot\mathrm{Im}^{-1}\left(1/q'_{\mathrm{noise}}\right) =$$
$$= -\lambda\cdot\mathrm{Im}^{-1}\left(1/\left(iC+l+z_{\mathrm{glass}}\right)\right) = \frac{\lambda}{C}\left(C^2+\left(l+z_{\mathrm{glass}}\right)^2\right),$$

resulting in the following:

$$\frac{A'_{\mathrm{peak}}}{A'_{\mathrm{noise}}} = \frac{C^2+2C^2\frac{l(N-1)}{z_{\mathrm{glass}}}+C^2\frac{l^2(N-1)^2}{z^2_{\mathrm{glass}}}}{C^2+\left(l+z_{\mathrm{glass}}\right)^2}+$$
$$\frac{z^2_{\mathrm{glass}}+2lNz_{\mathrm{glass}}+l^2N^2}{C^2+\left(l+z_{\mathrm{glass}}\right)^2}. \tag{10}$$

Appendix B. Beam area calculation for pulse peak versus noise as a function of the glass and iris positions

Here an optimal iris position (l) and glass position (z_{glass}) are calculated, according to the peak-to-noise beam areas ratio (the expressions were obtained in Appendix A). Inserting $N = 1-f_{\mathrm{NL}}/z_{\mathrm{glass}}$ to $A'_{\mathrm{peak}}/A'_{\mathrm{noise}}$ from Equation (10), Appendix A, results in the following:

$$\frac{A'_{\mathrm{peak}}}{A'_{\mathrm{noise}}} = \frac{\frac{C^2l^2}{f^2_{\mathrm{NL}}}-\frac{2C^2l}{f_{\mathrm{NL}}}+C^2+l^2\left(1-\frac{z_{\mathrm{glass}}}{f_{\mathrm{NL}}}\right)^2}{C^2+\left(l+z_{\mathrm{glass}}\right)^2}+$$
$$\frac{2lz\left(1-\frac{z_{\mathrm{glass}}}{f_{\mathrm{NL}}}\right)+z^2_{\mathrm{glass}}}{C^2+\left(l+z_{\mathrm{glass}}\right)^2}.$$

In addition, f_{NL} depends on z, according to the next equation:

$$\frac{1}{f_{\mathrm{NL}}} = \frac{8n_2d}{\pi w^4}P \Rightarrow$$
$$f_{\mathrm{NL}} = \frac{\pi}{8n_2dP}\left(w_0\sqrt{1+\left(\frac{\lambda z_{\mathrm{glass}}}{\pi w_0^2}\right)^2}\right)^4 =$$
$$= \frac{\pi w_0^4}{8n_2dP}\left(1+\left(\frac{z_{\mathrm{glass}}}{C}\right)^2\right)^2 = B\left(1+\left(\frac{z_{\mathrm{glass}}}{C}\right)^2\right)^2,$$

where $B = \frac{\pi w_0^4}{8n_2dP}$:

$$\Rightarrow A'_{\mathrm{peak}}/A'_{\mathrm{noise}}\left(z_{\mathrm{glass}},l\right) =$$
$$\frac{C^4l\left(C^4l-2B\left(C^2+z^2_{\mathrm{glass}}\right)\left(C^2+z_{\mathrm{glass}}\left(l+z_{\mathrm{glass}}\right)\right)\right)}{B^2\left(C^2+z^2_{\mathrm{glass}}\right)^3\left(C^2+\left(l+z_{\mathrm{glass}}\right)^2\right)}+1. \tag{11}$$

Moreover, the location of the new waist is as follows:

$$z_{w_{0,\mathrm{NL}}} = \left(z_{\mathrm{glass}}-f_{\mathrm{NL}}\right)\left(\frac{w_{0_{\mathrm{NL}}}}{w_0}\right)^2+f_{\mathrm{NL}},$$

where

$$w_{0_{\mathrm{NL}}} = \frac{w_0}{\sqrt{\left(1-z_{\mathrm{glass}}/f_{\mathrm{NL}}\right)^2+\left(\frac{2w_0^2}{\lambda f_{\mathrm{NL}}}\right)^2}}$$
$$\Rightarrow z_{w_{0,\mathrm{NL}}} = \frac{z_{\mathrm{glass}}-f_{\mathrm{NL}}}{\left(1-z_{\mathrm{glass}}/f_{\mathrm{NL}}\right)^2+\left(\frac{2C}{\pi f_{\mathrm{NL}}}\right)^2}+f_{\mathrm{NL}}.$$

The optimal iris position was obtained based on the schematic shown in Figure 5, Section 3. The value $z_{w_{0,\mathrm{NL}}}$ results in the minimal area ratio obtained in Equation (11). By inserting $l = z_{w_{0,\mathrm{NL}}}$ into Equation (11) one can obtain the optimal z_{glass} by finding the minimal area ratio. This can be done either by plotting it as a function of z_{glass} (Figure 8), or by taking its derivative expression and setting to 0.

Appendix C. Beam waist propagation inside the glass

In order to determine the shortest limit for $z_{w_{0,\mathrm{NL}}}$ where thin glass approximation is valid, a beam propagation method simulation[29] was used. The parameters that were considered were consistent with the numerical simulation parameters presented in Section 4.

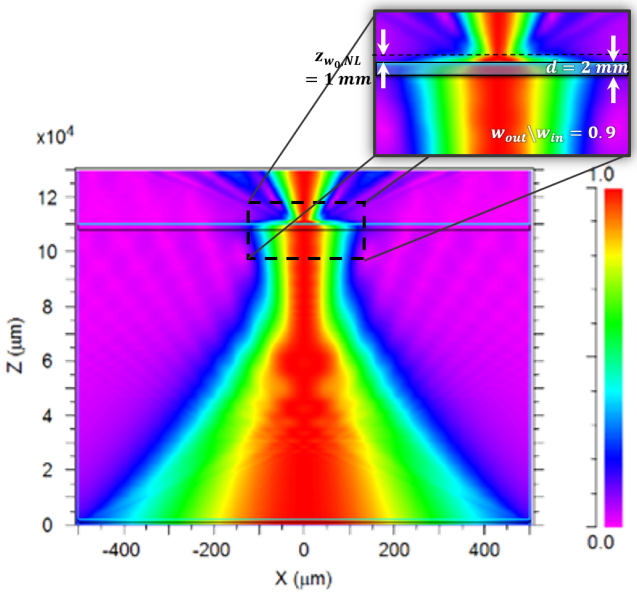

Figure 16. Beam propagation simulation showing spatial pulse variations. Starting from the bottom: beam convergence is observed after leaving the linear lens. A 'linear' waist is seen where the narrowest diameter is obtained (approximately the upper two-thirds of the figure). The nonlinear dielectric is represented by a cyan line. Major convergence occurs after leaving the nonlinear sample in air. The nonlinear waist is seen as the narrowest beam near the end (top).

As obtained from Figure 16, the beam diameter drops by 90% in the case where the glass thickness (d) is double the new formatted NL waist ($z_{w_0,\mathrm{NL}}$): $d = 2$ mm and $z_{w_0,\mathrm{NL}} = 1$ mm.

References

1. P. Maine, D. Strickland, P. Bado, M. Pessot, and G. Mourou, IEEE J. Quantum Electron. **24**, 398 (1988).
2. M. M. Murnane, H. C. Kapteyn, and R. W. Falcone, Phys. Rev. Lett. **62**, 155 (1989).
3. D. Neely, P. Foster, A. Robinson, F. Lindau, O. Lundh, A. Persson, C.-G. Wahlström, and P. McKenna, Appl. Phys. Lett. **89**, 021502 (2006).
4. J. P. Singh and S. N. Thakur, *Laser-induced Breakdown Spectroscopy* (Elsevier, 2020), p. 4148.
5. P. Sharma and R. K. Vatsa, *Materials under Extreme Conditions* (Elsevier, 2017), p. 575.
6. J.-P. Rousseau, R. Lopez-Martens, L. P. Ramirez, D. N. Papadopoulos, A. Pellegrina, F. Druon, P. Georges, A. Jullien, X. Chen, A. Ricci, J. P. Rousseau, R. Lopez-Martens, L. P. Ramirez, D. N. Papadopoulos, A. Pellegrina, F. Druon, and P. Georges, arXiv:1109.1992 (2011).
7. L. Shen, Y. Li, W. Li, J. Song, J. Qian, J. Sun, R. Feng, Y. Peng, and Y. Leng, High Power Laser Sci. Eng. **11**, e1 (2023).
8. J. Ma, P. Yuan, Y. Wang, H. Zhu, and L. Qian, Opt. Commun. **285**, 4531 (2012).
9. Z. Wang, C. Liu, Z. Shen, Q. Zhang, H. Teng, and Z. Wei, Opt. Lett. **36**, 3194 (2011).
10. Y. Huang, C. Zhang, Y. Xu, D. Li, Y. Leng, R. Li, and Z. Xu, Opt. Lett. **36**, 781 (2011).
11. G. Doumy, F. Quéré, O. Gobert, M. Perdrix, P. Martin, P. Audebert, J. C. Gauthier, J. P. Geindre, and T. Wittmann, Phys. Rev. E **69**, 026402 (2004).
12. M. P. Kalashnikov, E. Risse, H. Schönnagel, and W. Sandner, Opt. Lett. **30**, 923 (2005).
13. J. Liu, K. Okamura, Y. Kida, and T. Kobayashi, Opt. Express **18**, 22245 (2010).
14. X. Z. Wang, Z. H. Wang, Y. Y. Wang, X. Zhang, J. J. Song, and Z. Y. Wei, Chin. Phys. Lett. **38**, 074202 (2021).
15. X. Shen, P. Wang, J. Liu, and R. Li, High Power Laser Sci. Eng. **6**, e23 (2018).
16. N. Xie, X. Huang, X. Wang, K. Zhou, L. Sun, Y. Guo, and J. Su, J. Mod. Opt. **67**, 1314 (2020).
17. P. Zhu, A. Zigler, X. Xie, D. Zhang, Q. Yang, M. Sun, J. Papeer,J. Kang, Q. Gao, X. Liang, H. Zhu, A. Guo, Y. Liang, S. Ji, L. Ren, H. Liu, N. Kang,Y. Zhao, and J. Zhu, Opt. Lett. **45**, 2279 (2020).
18. P. L. Kelley, Phys. Rev. Lett. **15**, 1005 (1965).
19. A. L. Gaeta, Phys. Rev. Lett. **84**, 3582 (2000).
20. E. G. Lariontsev and V. N. Serkin, Soviet J. Quantum Electron. **5**, 796 (1975).
21. Z. Liu, L. G. Wright, D. N. Christodoulides, and F. W. Wise, Opt. Lett. **41**, 3675 (2016).
22. X. Shen, P. Wang, J. Zhu, Z. Si, Y. Zhao, J. Liu, and R. Li, Opt. Express **27**, 10586 (2019).
23. X. Lu and Y. Leng, Opt. Lett. **46**, 5108 (2021).
24. A. Weiner, *Ultrafast Optics*, Vol. 72 (John Wiley & Sons, 2011), p. 57.
25. M. J. Weber, D. Milam, and W. L. Smith, Opt. Eng. **17**, 463 (1978).
26. F. Verluise, V. Laude, Z. Cheng, C. Spielmann, and P. Tournois, Opt. Lett. **25**, 575 (2000).
27. A. Bendib, K. Bendib-Kalache, and C. Deutsch, Laser Particle Beams **31**, 523 (2013).
28. J. H. Marburger, Prog. Quantum Electron. **4**, 35 (1975).
29. https://www.synopsys.com/photonic-solutions/rsoft-photonic-device-tools/passive-device-beamprop.html.
30. C. Hooker, Y. Tang, O. Chekhlov, J. Collier, E. Divall, K. Ertel, S. Hawkes, B. Parry, and P. P. Rajeev, Opt. Express **19**, 2193 (2011).
31. C. Danson, D. Neely, and D. Hillier, High Power Laser Sci. Eng. **2**, e34 (2014).
32. J. Buldt, M. Mueller, R. Klas, T. Eidam, J. Limpert, and A. Tünnermann, in *Advanced Solid State Lasers* (2017), paper JM5A-25.
33. S. A. Self, Appl. Opt. **22**, 658 (1983).
34. www.ultrafast-innovations.com.
35. P. A. Bélanger, Opt. Lett. **16**, 196 (1991).